Imaging analysis of boundary layer combustion with tangential and radial oxidizer injection in a cylinder

Kei Obata*, Toru Shimada* and Koki Kitagawa*
*Institute of Space and Astronautical Science, JAXA
*Sagamihara City, Kanagawa 252-5210, JAPAN

Abstract
A small hybrid rocket engine has been developed, which has radial and swirl two hollow injectors, a large quarts glass window, a transparent combustion chamber and a divergent nozzle. Flame behaviors under atmospheric pressure combustion have been taken by high-speed photography with 30,000 FPS. The proper orthogonal decomposition (POD) is applied to the luminous intensity of acquired images. The higher POD modes are found to capture the structures of luminous flame streaks and the peak frequency of mode 2 coefficient is found to have some relation with the oscillation frequency of the boundary layer.

1. Introduction

Boundary-layer combustion is a combustion process specific to hybrid rocket. While hybrid rocket is promising as a future space transportation technology due to its simple structure, safety and environmental compatibility, it has not yet been used in practice mainly due to the following disadvantages caused by boundary-layer combustion: (1) low fuel regression rate, (2) combustion instability, (3) low combustion efficiency caused by poor mixing of oxidizer and fuel, which is evident in the case of liquid oxidizer injection, (4) shift of oxidizer-fuel mixture ratio (O/F) from the optimum value by the thrust control, which leads to the fuel residue.

In order to increase fuel regression rate, convective heat transfer from the flame to the fuel grain surface needs to be enhanced. Swirling-Oxidizer-Flow-Type (SOFT) hybrid rocket (HR) engine is developed and it increases the fuel regression rate of PMMA up to about three times in comparison with conventional HR engine[1]. The centrifugal force of the swirling motion increases the pressure near the fuel grain surface and boundary layer thickness may be reduced as a result. This reduces the time lag of heat transfer between flame and fuel so that combustion stability is improved. Swirling oxidizer flow also promotes the mixture of fuel gas and oxidizer. SOFT HR is capable of solving first three problems of hybrid rocket as mentioned above and "gaseous oxidizer injection" is the key to these great effects of swirling flow. Kitagawa et al studied fuel regression rates, C^* efficiency and specific impulse of the HR engine with swirling LOX flow and they were found to be smaller than those with swirling gaseous oxygen (GOX)[2]. Altering-intensity Swirling-Oxidizer-Flow-Type (A-SOFT) HR engine has been proposed as those developed SOFT HR engine[3]. It has both axial and tangential oxidizer injections and can manipulate swirl intensity. So it is expected that it can control O/F and thrust simultaneously by manipulating both total mass flux of oxidizer and swirl intensity independently. Then last technical problem of hybrid rocket is cleared by A-SOFT's dual injection. Finally A-SOFT is thought to resolve all four technical problems of hybrid rocket at once.

The understanding of its combustion process is needed for the practical use and the optimal design of a hybrid rocket engine. The visualization of flames in combustion chamber is considered to be useful and a lot of experiments have been done before. Jens et al studied the location of the flame in a turbulent boundary layer over a solid fuel by using simultaneous Schlieren and OH* chemiluminescence imaging[4]. The flow configuration was representative of a hybrid rocket engine. For about SOFT HR engine, Yuasa et al observed the swirling flame structure and the averaged flame zone thickness on the grain surface in previous research[5]. However, visualization experiment for hybrid rocket engine with both tangential and radial oxidizer injection has not yet been done.

Thus, in this research we try to capture the flame behavior and apply image processing to them in order to know the effect on the combustion field of the changes in tangential to radial oxidizer flow ratio. For this experiment, a small A-SOFT HR engine has been developed, which has radial and swirl two hollow injectors, a large quarts glass window and a transparent combustion chamber. The oxidizer flow coming out of the 8 slits of the radial injector will be combined and crate an axial flow. This formation of injector slits was used to make a non-swirling flow in Ref.5. Then the flame behavior was captured by high-speed photography with the change of tangential to radial oxidizer

flow ratio. Elementary image analysis was applied to the flame images to obtain axial distribution of angles of swirling flame streaks and flame zone thickness. From these results, the difference of flow field in different swirl intensities was examined. The proper orthogonal decomposition was also applied to the acquired images. The dominant flame structure in combustion chamber and the frequency of its change were discussed using POD modes and POD mode coefficients.

2. Experimental Setup and Proceeding

2.1 Experimental Setup

Figure 1 shows a schematic of the rocket engine and high-speed camera system used in this experiment. It mainly consisted of a hybrid rocket engine, a gas oxygen supply system, flame observing devices and operation system. For this experiment we made a new type of small hybrid rocket engine shown in Fig.2. This engine has both radial and swirl injectors, a solid fuel grain made of transparent acrylic (PMMA), and a large quartz glass window to directly observe the combustion chamber from the front. A fuel grain length and a diameter are 150mm and 40mm. This engine also has a divergent nozzle instead of a convergent nozzle. It is because throttling the passage of the combustion flow by throat will affect the development of boundary layer and the form of the flow and flames. How combustion flow looks like will be different depending on whether the engine has a convergent nozzle or not especially when observing from the front. At first we try to gain the knowledge of combustion flow with no convergent nozzle and after that go to analysis of combustion flow with convergent nozzle. From both the front and side of the combustion chamber, flame behavior can be captured by two high-speed cameras.   The photographic conditions are as follows: the high-speed camera used in this study is HX3 series of NAC Image Technology, frame rate is 30,000 fps, exposure time is 1/30,000 s, f-number is changed depending on the experimental conditions to avoid saturation. Flame behavior was captured for about 2.5 seconds from 3 seconds after opening the main valve.
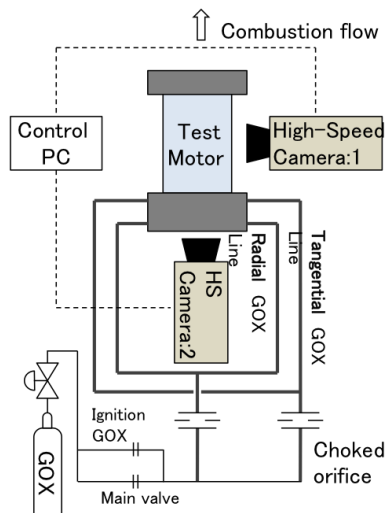
Figure 1: Schematic of experimental setup using high-speed camera
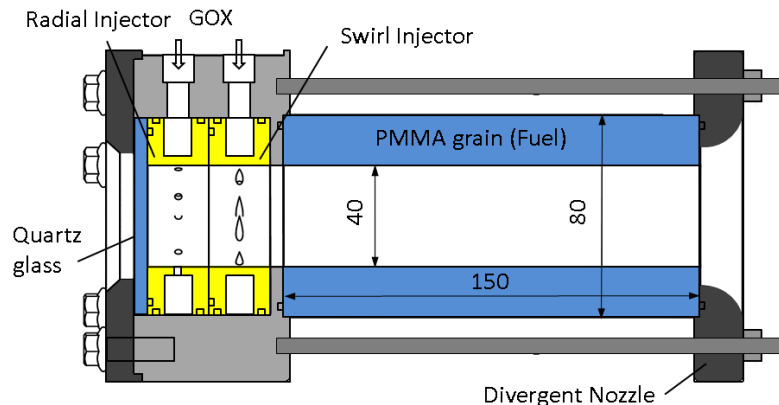
Figure 2: Schematic of the hybrid rocket engine for flame visualization

Figure 3 shows the injectors used in this study. For the swirl injector, the swirl intensity of the oxygen jet is characterized by the geometrical swirl number of the injector[6][1]. In this experiment, the swirl injector which has Sg of 30.0 is used. It has eight tangential slits to make homogeneous swirling flow. The radial injector also has eight radial slits.
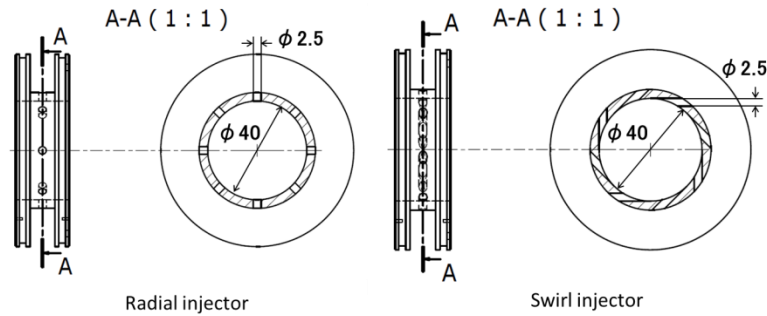
Figure 3: Schematic of injectors

2.2 Experimental Proceeding

Figure 4 shows the ignition method of this experiment. In the burning test, the nichrome wire is used for ignition. The nichrome wire was fixed at 10mm from the trailing edge of the fuel grain. This is because the nichlome wire fixed at upstream is found to disturb the downstream flow early in this experiment. The nichrome wire is heated and a small amount of GOX (0.11g/s) continues to be supplied until flame propagated to the leading edge of the grain. Then the main valve is opened. Experimental conditions are listed in Table 1.
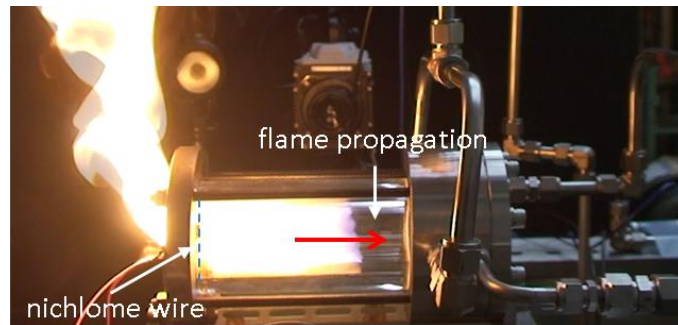
Figure 4: The photograph of ignition method

Table1: Experimental conditions

GOX supply pressure [MPa]	0.5				
GOX mass flow rate [g/s]	6.3				
Tangential to radial GOX flow ratio (T/R) [-]	0.0	0.7	1.4	3.1	∞
Swirl intensity (Se) [-]	0.0	1.8	5.3	10.1	30.0
GOX supply time [s]	6				

In this study the experimental variable is only the effective geometric swirl number Se. GOX mass flow rate is fixed to 6.3 [g/s] and tangential to radial oxidizer flow ratio is varied in 5 setting values (hereinafter, this ratio is called T/R). GOX supply time is constantly 6s. Radial and tangential oxidizer flow rates are controlled by choked orifice.

---

[1] Assuming that oxygen is injected uniformly through inlet holes of the injector and the axial oxygen velocity distribution is also uniform over the injector exit, a geometric swirl number S_g can be defined in terms of the geometry of the injector by considering the conservation of momentum, using the following equation:

$$S_g = \frac{\pi(R-r)R}{\pi n r^2} \qquad (1)$$

Kei Obata, Toru Shimada and Koki Kitagawa

In A-SOFT hybrid rocket, the swirl intensity of the oxygen jet is characterized by Se instead of Sg. The effective geometric swirl intensity is defined as:

$$S_e = \frac{S_g}{(1 + \dot{m}_{oa}/\dot{m}_{ot})^2} \tag{2}$$

where Sg is the geometric swirl number of the injector (Sg=30.0), $\dot{m}_{oa}$ is the muss flux of radial oxidizer, and $\dot{m}_{ot}$ is that of tangential oxidizer. In the case of $\dot{m}_{oa} = 0$ that is only tangential oxidizer flow condition, Se equals to Sg.

3. Proper Orthogonal Decomposition

Proper orthogonal decomposition (POD) is a decomposition technique which can extract several low order components from the data with huge number of dimensions. POD can find "appropriate" bases to efficiently express the given data with small number of dimensions. POD has been widely used to extract coherent structure in a turbulent flow field[7], and these days, it is used for analysing combustion instability[8].

Suppose $\{x_t\}$ is the time series data set. Here each element in the data set $\{x_t\}$, $t = 1, 2, \ldots, N$ is an image composed of n by m pixels, where the index t describes a time sequence of images. POD extracts time-independent orthonormal basis functions φ_i and time-dependent orthonormal amplitude coefficients $c_{i,t}$. The reconstruction of $\{x_t\}$ with the first r modes, $r \leq N$:

$$x_t \approx \tilde{x}_t = \sum_{i=1}^{r} c_{i,t}\, \varphi_i \tag{3}$$

is optimal with respect to minimizing the following quantity:

$$\varepsilon_r = \sum_{t=1}^{N} \|x_t - \tilde{x}_t\|^2 \tag{4}$$

The method of snapshots is convenient when the number of collected samples is smaller than the space discretization, that is, $n \cdot m = M \gg N$[9]. The first step consists in calculating a $N \times N$ covariance matrix K from data elements $\{x_t\}$:

$$K = \sum_{t=1}^{N} x_t^T\, x_t = X^T X \in \mathbb{R}^{N \times N} \tag{5}$$
$$\text{where } X = [x_1, \ldots, x_N] \in \mathbb{R}^{M \times N}$$

Then an eigenvalue problem of **K** is solved and the mode φ_i is constructed by linear combination of the N images according to the eigenvectors v_i:

$$K v_i = \lambda_i v_i \tag{6}$$

$$\varphi_i = \frac{1}{\sqrt{\lambda_i}} \sum_{t=1}^{N} x_t\, v_i = \frac{1}{\sqrt{\lambda_i}} X\, v_i \tag{7}$$

The projection of $\{x_t\}$ onto φ_i generates the temporal coefficients $c_{i,t}$:

$$c_{i,t} = \langle x_t, \varphi_t \rangle \qquad t = 1, \ldots, N \tag{8}$$

Then $\{x_t\}$ can be approximated by a linear combination of the first r modes as Eq. (3). POD modes are ordered according to decreasing magnitude of their corresponding (real, positive) eigenvalues λ_i. Usually cumulative correlation energy is defined as:

$$E_r = \sum_{i=1}^{r} \lambda_i \bigg/ \sum_{i=1}^{N} \lambda_i \tag{9}$$

The number of r is determined so that E_r becomes sufficiently close to 1.

4. Result and Discussion

4.1 Experimental Result

4.1.1 Combustion flow structure in combustion chamber

   Figure 5 shows a typical image (at 3sec after opening the main valve) of burning PMMA grain taken by high-speed photography from the front. Whole grain surface can be observed from the view of this image and the location of the grain edge of nozzle side is shown by the white broken line. Figure 6 shows three photographs of PMMA combustion with both tangential and radial oxidizer injection. Swirling flames formed in the combustion chamber. Swirling small striated flames shown in Fig.7 also confirmed the formation of swirling flames. These small striated flames were found to be formed near the depressions inner surface of the grain developed toward the swirl direction of the O_2 flow[5]. Here luminous flame is targeted instead of flame at equivalent ratio to analyse the flame structure.
   Figure 7 and 8 show the side view of the combustion chamber in different swirl intensities. Swirling small striated flames are designated as black dotted lines. In the case of Se=10.1 the swirling small striated flames formed over the whole area of the grain as with the case of only tangential oxidizer injection (Se=30.0). In the case of Se=5.3 and Se=1.8, swirling flames formed in the area up to the midstream and upstream respectively. In the case of Se=0.0 swirling flames didn't form. From these facts it is assumed that only in the case of high Se number combustion flow fully rotates in the combustion chamber and goes out, while its axial velocity is increased by the mass addition of blowing fuel gas. In this experiment when the T/R ratio is over 3.1 (in the case of Se=10.1 and Se=30.0), a sufficient swirling effect is obtained.
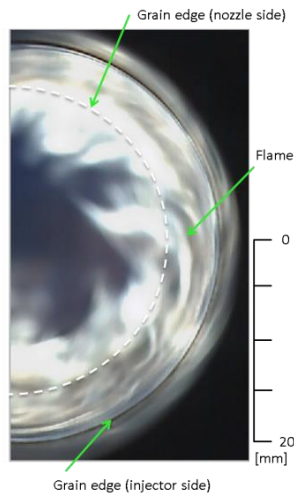
Figure 5: Flame appearance with both tangential and radial oxidizer injections in burning PMMA grain, GOX=6.30[g/s], O/F=1.66
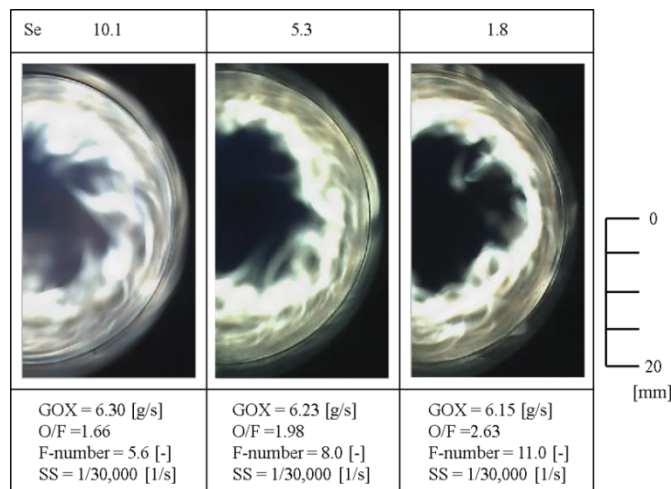
Figure 6: Flame appearance with both tangential and radial oxidizer injections in burning PMMA grain in three conditions

Kei Obata, Toru Shimada and Koki Kitagawa
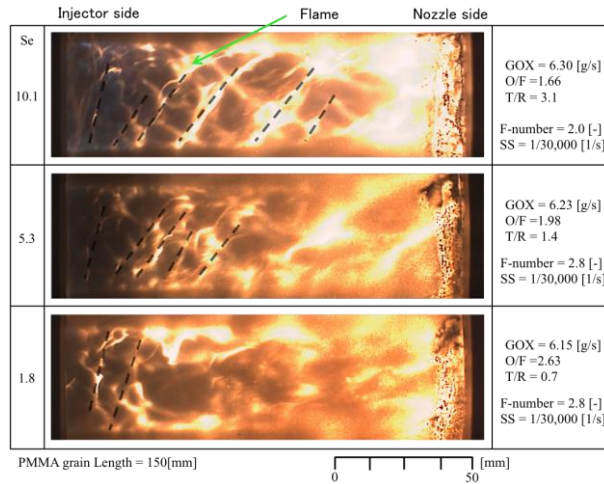
Figure 7: Flame appearance with both tangential and radial oxidizer injections in the combustion chamber from the side view in three conditions
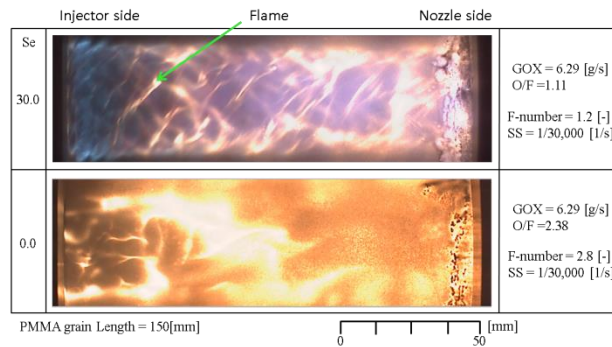
Figure 8: Flame appearance with only tangential and radial oxidizer injection in the combustion chamber from the side view

Figure 9 shows the axially distribution of angles of swirling flame streaks. It is obtained by applying elementary image analysis to the side image of the combustion chamber as shown in figure 7 and 8. The images for which image analysis is performed are taken 3 second and 4 second after opening the main valve in the case of Se=30.0, 10.1 and 5.3. Sampling rate is 0.01s and the number of sample images is 20 in each case. At first, RGB flame image is converted to the grayscale image. For each pixel of grayscale image the difference in luminous intensity between adjacent pixels ($\Delta I_x, \Delta I_y$) is calculated and then ΔI is obtained from equation (10).

$$\Delta I(x, y) = \sqrt{\Delta I_x{}^2 + \Delta I_y{}^2} \tag{10}$$

Considering the pixel which has large ΔI represents the edge of the flame, we select pixels in order from biggest ΔI up to the top 7% of entire pixels and binary image is obtained by the threshold, which is the minimum ΔI of selected pixels. Figure 10 shows the binary image obtained by image analysis. To this image approximated straight lines are manually drawn along the edge of the frame and angles of these lines and location of intersection point of grain center is measured. This process is performed on each 20 images and the average angle of every 10mm from the leading edge of the grain is plotted as shown in figure 9.

The angles of swirling flame streaks decrease in inverse proportion to the axial location from the leading edge of the grain. In figure 9 we can see two decreasing curves in each swirl number, a rapid decreasing curve and a gradual decreasing curve. The intersection point of these two decreasing curves moves to the injector side as the Se number increase (hereinafter, this intersection point is called inflection point). In the region of a rapid decreasing curve, it is assumed that the ratio of tangential to axial velocity of combustion flow rapidly decreases as the increase in its axial velocity and then angles of swirling flame streaks rapidly decreases. The rapid increase in the mass of fuel gas causes this phenomenon. While in the region of gradual decreasing curve, fuel regression rate is comparatively low and total mass flow rate of oxidizer and fuel gas is expected to increase gradually at a constant pace. Thus the angles of swirling flame streaks gradually decrease as the axial velocity gradually increases. The development of boundary layer is more rapid in higher Se number and the location where the fuel regression rate is decreased to a constant

value is closer to the leading edge of the grain. This causes the inflection point to move to the injector side. The rapid decreasing curve is the same regardless of the Se number. This is because the decrease in angle of swirling flame streak is affected by both the increase in the axial velocity and the initial value of the tangential velocity of oxidizer. The initial tangential velocity is proportional to the mass flow rate of the swirl injector, and the ratio of this mass flow rate between 3 conditions is (Se=30.0, 10.1, 5.3) = (1.0, 0.76, 0.58) in this experiment. It is also confirmed that the angle of swirling flame streak becomes larger as the Se number increase.
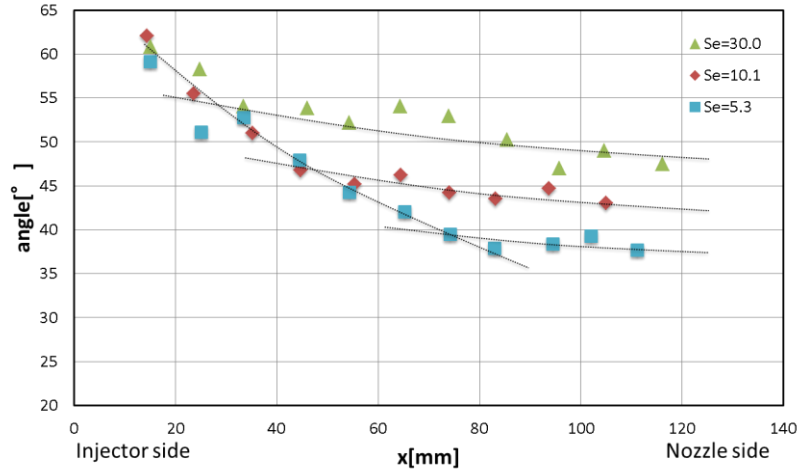
Figure 9: Axially distribution of angles of swirling flame streaks
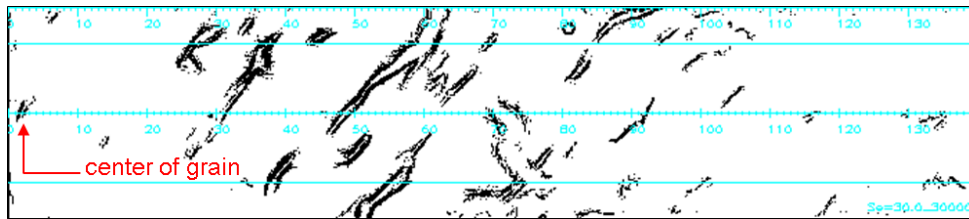
Figure 10: Binary image of flame appearance in the combustion chamber from the side view

4.1.2 Fuel regression rate

   The time and axially averaged fuel regression rate is shown in Fig.11. Fuel regression rate is the maximum in the case of only tangential oxidizer injection (Se=30.0) and it decreases as the effective swirl number decreased. Fuel regression rate is greatly affected by the change of the tangential to radial oxidizer flow ratio.

   Fuel regression rate was compared between the experimental results and the approximated model in Figures 11 and 12. In this research, the axially averaged fuel regression model is adopted as

$$\dot{r} = a_0(1 + S_e^2)^m G_0^n \tag{11}$$

where a_0 , m and n are experimental coefficient, G_0 is the time averaged mass flux of oxidizer. The term $(1 + S_e^2)^m$ refers to the dependence of swirling flow to the conventional hybrid combustion regression rate formula as $\dot{r} = a_0 G_0^n$ in Ref. 5). The values of a_0, m and n are determined by the least square minimization method. Mass flux of oxidizer G_0 can be considered as fixed value ($G_0 \approx 4.588$) because its variance is so small. The exponent n is considered to be in the range 0.5-0.8 in Ref. 10). Under these conditions a_0, m and n are determined and the axially averaged fuel regression model is expressed as follows:

$$\dot{r} \, [mm/s] = 0.029(1 + S_e^2)^{0.166} G_0^{0.650} \tag{12}$$

   Figures 11 and 12 show that the fuel regression rate has dependence on effective geometric swirl number, and fitting model as shown in Eq. (12) fits the experimental fuel regression rate reasonably well. This result suggests that fuel regression rate can be controlled by manipulating tangential to axial oxidizer flow ratio. In our research group, static firing experiment of A-SOFT HR engine was done by Ozawa et al in 2016[11]. In that experiment fuel regression rate of burning PP grain under pressurized combustion was measured with the change of both the swirl

Kei Obata, Toru Shimada and Koki Kitagawa

intensity and the total mass flux of oxidizer. Axially averaged fuel regression model of that previous experiment was defined using these constants $(a_0, m, n) = (0.026, 0.099, 0.651)$. Approximated model got in this experiment is very similar to that of static firing experiment. The contribution of swirling flow to regression rate is a little larger in this time. This difference is thought to attribute to the materials of fuel and whether pressurized or not, however further examination is needed in this point. It is necessary to investigate the fuel regression rate of burning PMMA fuel grain under pressurized combustion in the future experiment. The effect of total mass flux of oxidizer is also investigated.
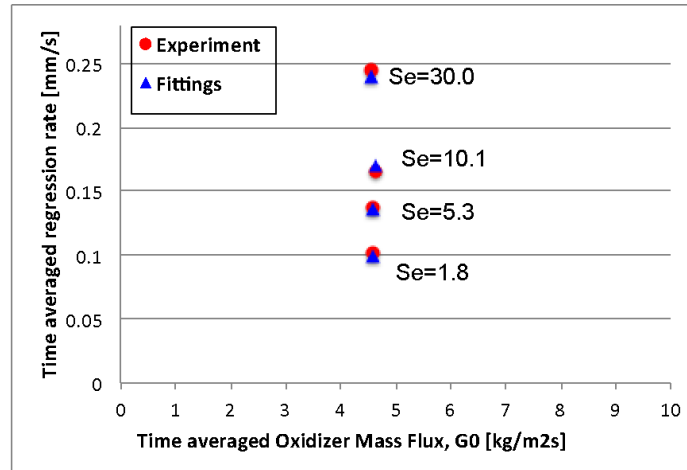
Figure 11: Comparison of the time and axially averaged regression rate of the visualization experiments of A-SOFT HR with the results of the fitting of Eq. (12); PMMA grain, atmospheric pressure combustion
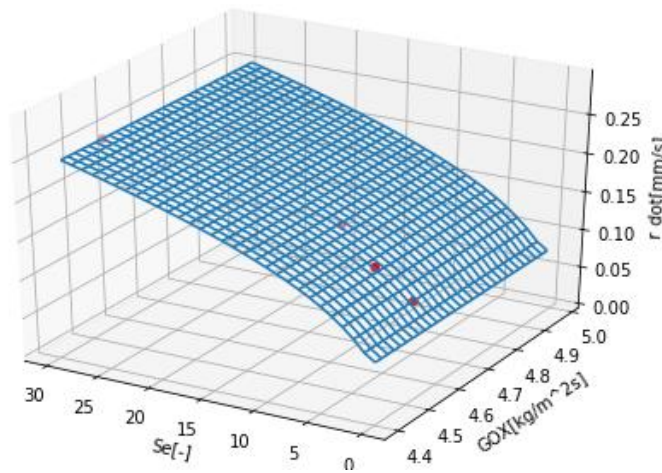
Figure 12: Comparison of the approximation of the fuel regression rate with the results of the visualization experiment of A-SOFT HR

4.2 Result of Image analysis

4.2.1 Flame zone thickness

Flame zone thickness is quantitatively measured from the mean field of luminous intensity of 300 images taken from the front. Here, flame zone thickness is defined as the thickness in radial direction of the area where the luminous flame is formed. Burnt gas and unburnt gas coexist in the center of the combustion chamber. However, they can't be distinguished by the visible sight because of the strong emission of luminous flames. Here, this area is defined as non-luminous area. 300 images taken 3 second after opening the main valve, which corresponds to 10ms, are used in this analysis. Even in the case of Se=30.0 with the maximum fuel regression rate, the change in diameter $(\Delta D / D_0)$ during this time is about 0.01%.

Figure 13 shows the mean field of luminous intensity of 300 images and distinction between flame zone and non-luminous area in the case of Se=10.1. Assuming that the combustion flow is axisymmetric, the angle of view is only

half of the grain. The spatial resolution of the image is 0.06mm/pixel. Flame zone and non-luminous area are
distinguished by the predetermined threshold of luminous intensity. The threshold is set to 64 for the case of Se=30.0
and 144 for the other cases. In the case of Se=30.0, the flame emission was weak and even the maximum luminous
intensity was 100.1. The ratio between the threshold and the maximum luminous intensity is set to about the same
value 0.6 ~ 0.64 in all cases. Non-luminous area whose luminous intensity is less than the threshold corresponds to
the black area in the center of the grain. The equivalent circle diameter is calculated from the area of this region, and
the length subtracted from the grain radius is taken as the flame zone thickness. Figures 14 and 15 show the mean
field of luminous intensity and flame zone thickness in different swirl intensities. The flame zone thickness increases
as the Se number increases except for the case of Se=1.8. Assuming that luminous flame seems to be located within
the boundary layer, the boundary layer is assumed to become thicker as Se number increases. The flame zone
thickness of burning PMMA is in the range of 7mm~10mm, which is larger than that of swirling-oxidizer-flow-type
hybrid rocket engine in the previous research (4mm~8mm)[5]. In the previous research PMMA grain with same inner
diameter was used, however, it was burned under pressurized condition and mass flow rate of oxidizer was more than
3 times. The boundary layer thickness was thought to be smaller than that of this experiment. Thus the flame zone
thickness obtained in this analysis seems to be reasonable. The flame zone thickness in the case of Se=1.8 is smaller
than that of Se=0.0. In the case of Se=1.8, the swirl intensity of combustion flow was thought to be too weak and
flow field was similar to that of only radial oxidizer injection. In this point further examination is needed in the
future.
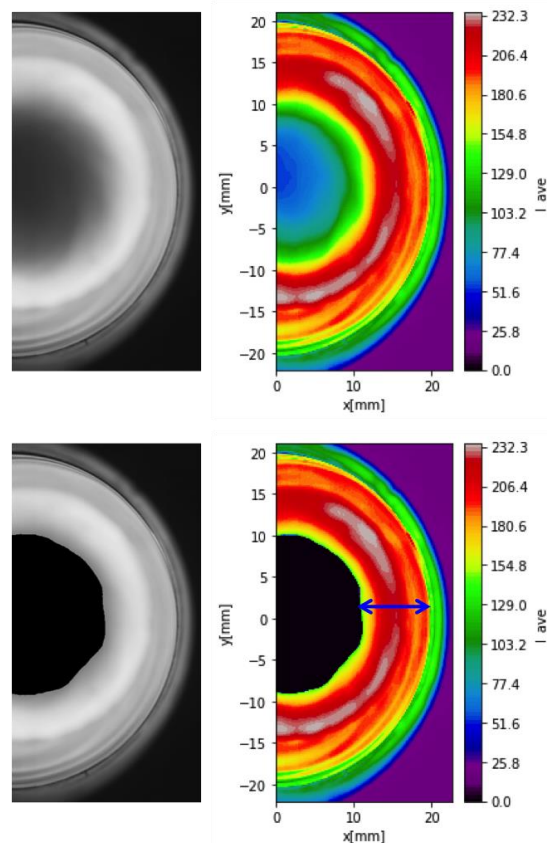
Figure 13: The mean field of luminous intensity of 300 images (top) and distinction between flame zone and non-
luminous area (bottom), Se=10.1. Blue double arrow line roughly shows the flame zone thickness.

Kei Obata, Toru Shimada and Koki Kitagawa
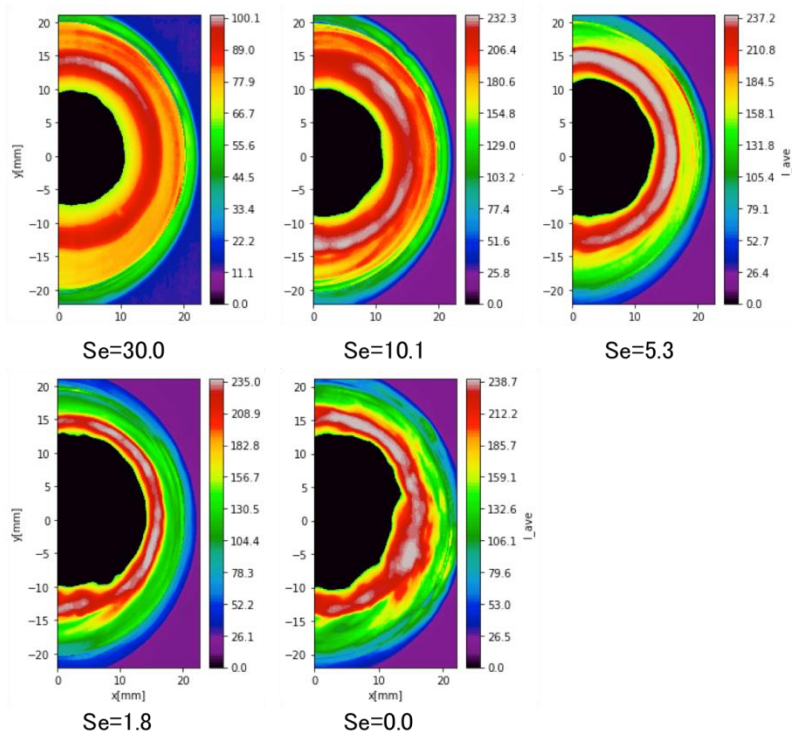
Figure 14: The average luminous intensity field of 300 images in different swirl intensities
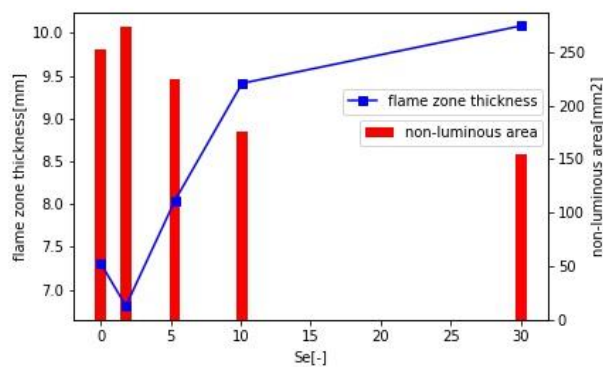
Figure 15: Flame zone thickness and non-luminous area

4.2.2 Result of POD analysis

POD is applied to the analysis of images of luminosity taken from the side. The size of the image is $152\text{pix} \times 715\text{pix}$ and this corresponds to the region of $0\text{mm} \leq x \leq 136\text{mm}, -14.5\text{mm} \leq y \leq 14.5\text{mm}$. 3,000 images taken 3 second after opening the main valve, which corresponds to 100ms, are used in this analysis. Here, the POD basis (mode) obtained by POD analysis is named mode 1, mode 2,…, in the order of energy which occupies.

Figures 16 and 17 show the mean field of luminous intensity of 3,000 images and the distribution of luminous intensity represented by POD mode 1 in the case of Se=30.0. The contour indicates the distribution of luminous intensity, where the red side is the high luminous intensity area and the black side is the low luminous intensity area (similarly in the result of POD mode after Fig.18). In figure 16 the luminous intensity of mean field is directly used and the values obtained when the mode is normalized are used in the figures showing the results of POD mode after figure 17. Comparing figure 16 with figure 17, POD mode 1 seems to extract the distribution of luminous intensity of mean field because the two figures look very similar to each other. In this study POD analysis is directly applied to the image luminous intensity data, however, in some cases POD is applied after subtracting the average value from the luminous intensity data[12]. In that case it seems that a mode which represents the mean field doesn't appear.

Figure 18 shows some higher order POD modes. Both the mode 2 and mode 3 structures seem to capture flame streaks towards the upper right (hereinafter, this structure is called pattern A). These flame streaks are formed over the inner surface of the grain on the side close to the camera. While the structures of mode 2 and 3 look very similar

to each other, the position which indicates the peak is slightly different, that is, the spatial phase is different. From these facts, mode 2 and mode 3 seem to capture the different flame streak. The mode which has the same structure as pattern A appears consecutively until mode 9 and then mode 10 and mode 11 first represent different structure from pattern A. The structure of these modes seem to capture flame streaks towards the lower right (hereinafter, this structure is called pattern B). These flame streaks are formed over the inner surface of the grain on the side far from the camera. Mode 10 and mode 11 also seem to capture the different flame streak.

Figure 19 shows the comparison of POD mode 2 among 3 different swirl intensities. All of them show the structure of pattern A. The angles of structure representing the flame streak increase, as the Se number increase. This tendency is consistent with the fact that the angle of swirling flame streak becomes larger as the Se number increase, which is reported in the section 4.1.1. This fact confirms that higher order POD modes capture the structure of the flame streak. POD modes which show the structure of pattern B also appear in the case of both Se=10.1 and 5.3. In the case of Se=1.8 and 0.0, POD mode indicating the structure of pattern A and B doesn't appear.
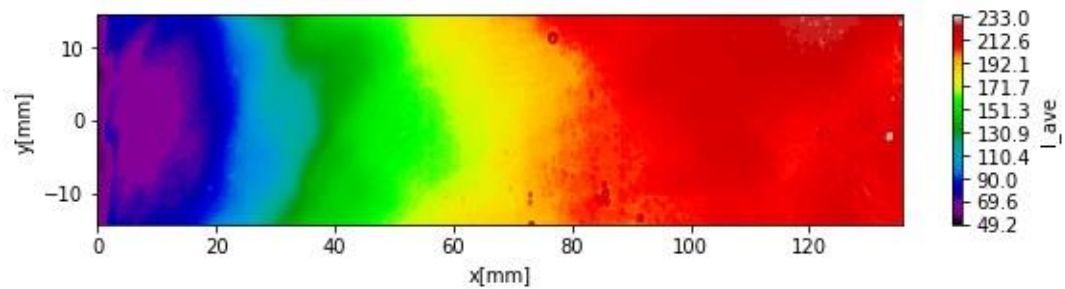
Figure 16: The mean luminous intensity field, Se=30.0
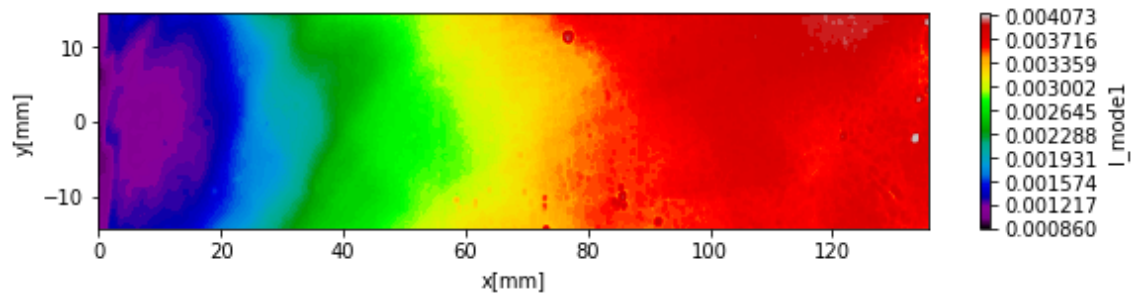
Figure 17: First POD mode, Se=30.0
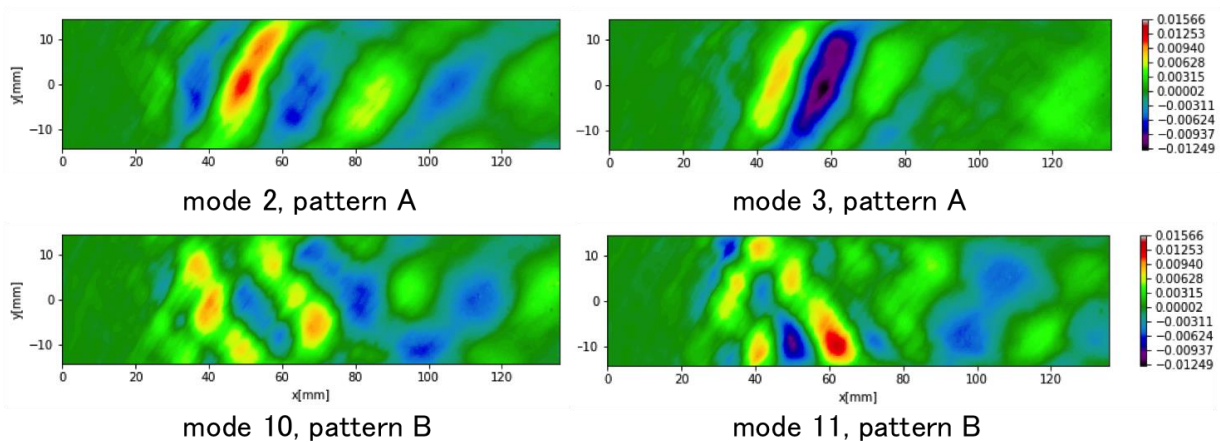
Figure 18: Some higher order POD modes, Se=30.0
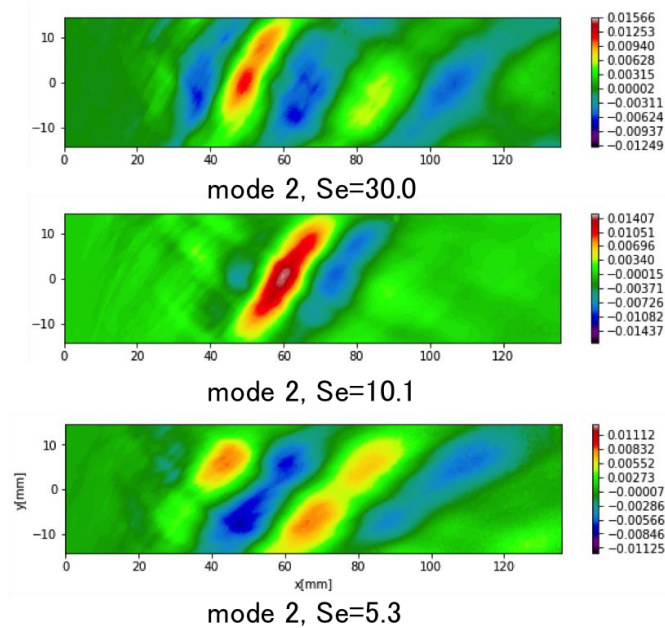
Figure 19: Comparison of POD mode 2 among 3 different swirl intensities

Figure 20 shows the energy ratio of each POD mode and the cumulative contribution ratio in the case of Se=30.0. Mode 1 occupies a very large proportion because it extracts the mean field luminous intensity. From the viewpoint of energy, the field of luminous intensity can be restored 99.0% by only 21 modes out of all 3,000 POD modes. The distribution of luminous intensity of combustion field can be expressed by a small number of POD modes. Figure 21 shows the energy ratio of TOP 15 POD modes in the case of Se=30.0. Mode 2 and mode 3 indicating pattern A mentioned above have energy of about 1.8 times that of mode 10 and mode 11 which show the structure of pattern B. This difference is thought to attribute to the difference in absolute luminous intensity of luminous flame due to the distance from the camera. Modes having almost the same energy appear in succession, as with mode 2 and mode 3, mode 4 and mode 5, mode 8 and mode 9, and mode 10 and mode 11. It is known that when temporally periodic physical phenomena are analysed by POD, the POD modes which have almost the same energy appear as pairs two by two[13]. In this research, like mode 6 and mode 7, independent mode which is not paired is inserted between them. The existence of mode which does not have such a pair is also pointed out in Ref.14.
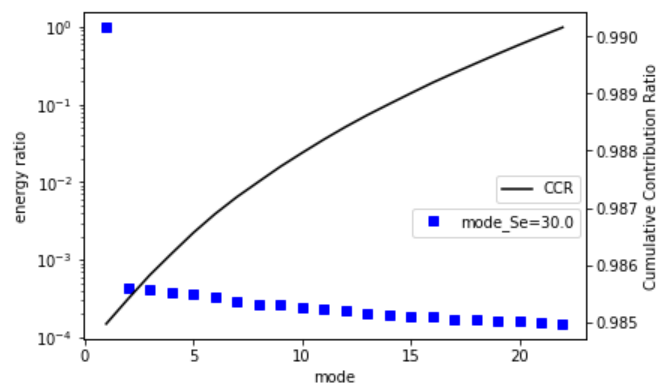
Figure 20: The energy ratio of each POD mode and the cumulative contribution ratio, Se=30.0
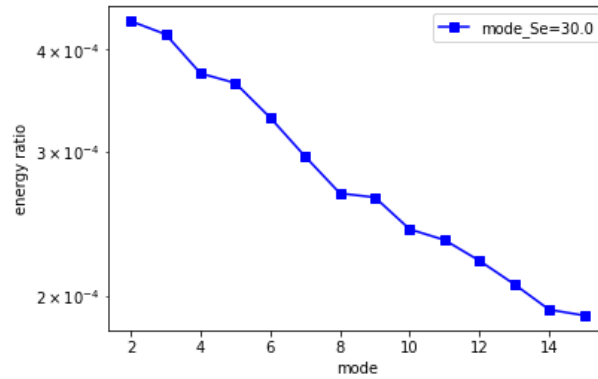
Figure 21: The energy ratio of Top 15 POD modes, Se=30.0

Figure 22 shows the time history of mode 2 and mode 3 coefficient in the case of Se=30.0. It seems that mode
coefficients of two modes periodically change and the temporal phase is different. Figure 23 shows the result of Fast
Fourier Transformation to the mode 2 coefficient in different swirl intensities. The vertical axis of the figure
represents the amplitude normalized by the maximum value. The mode 2 coefficient of Se=30.0 has apparent peaks
at 249.0 Hz, 395.5 Hz, 512.7 Hz and 615.2 Hz and the amplitude reaches its maximum at 512.7 Hz. In the case of
Se=10.1 and 5.3 the peak frequency seems to decrease a little compared to the case of Se=30.0. In the case of Se=1.8
the peak frequency becomes around 130 and less high frequency appears. The peak frequencies of the mode 2
coefficient in different swirl intensities are listed in the second row of Table 2. In this experiment, there is a general
tendency that the peak frequency of mode 2 coefficient becomes large as the Se becomes large. Regarding the case of
Se = 0.0, the peak frequency of the mode 3 coefficient is represented. This is because the mode 2 is an independent
mode and the peak frequency of mode 2 coefficient is considerably lower than that of other modes.

These mode 2 frequencies are considerably lower than the frequency at which the swirling oxidizer flow rotates the
inner surface of the grain and the frequency of the acoustic vibration, thus mode 2 is thought to have no relation with
these phenomena. As mentioned above, mode 2 is the mode which captures periodic changes in luminous intensities
of luminous flames. Generally, in the boundary layer combustion, the flame surface where the equivalent ratio is 1.0
exists in the boundary layer[15]. Since it is considered that the luminous flame is formed near the inner surface of the
fuel grain where the equivalent ratio is larger than 1.0, the luminous flame is thought to be affected by the vibration
of the boundary layer. Thus we assume that the frequency of mode 2 coefficient is somehow related to the oscillation
frequency of the boundary layer. The primary hybrid oscillation frequency is defined as equation (13) in Ref.16:

$$f = 0.234\left(2 + \frac{1}{O/F}\right)\frac{G_0 RT_{av}}{LP_c} \tag{13}$$

where $RT_{av} = 6.38 \times 10^5 (m/s)^2$ for GOX systems, L is the length of the fuel port, Pc is the average chamber
pressure, G_0 is time averaged total mass flux of oxidizer. The frequency obtained by assigning the value of this
experiment to each parameter of equation (13) is listed in the third row of Table 2. The fourth row in Table 2 shows
the ratio of the peak frequency of the mode coefficient to this frequency. In the case of Se=1.8 and 0.0, which is the
case of almost non-swirling flow, this ratio is close to 1.0. This ratio becomes large as the Se number increases.
Assuming that the equation (13) is an empirical formula applied to the axial flow type hybrid rocket, with the
increase in swirl intensity, the oscillation frequency of the boundary layer is expected to become larger than the value
obtained by equation (13). This is because the oscillation frequency of the boundary layer and the boundary layer
delay time (τ_{bl2}) has an inverse proportional relationship as shown in equation (14):

$$f = 0.48/\tau_{bl2} \tag{14}$$

The delay is thought to depend on the diffusion time scale across the boundary layer, $\tau_{bl2} \cong \delta/U^*$. Since the
diffusion speed U^* is expected to become larger as the swirl intensity increases, the delay time is expected to become
shorter. The fifth row in Table 2 shows the estimated delay time obtained by assigning the peak frequency of the
mode 2 coefficient into equation (14). In the case of only tangential oxidizer injection, the boundary layer delay time
becomes four times at the maximum shorter than that of the case of only radial oxidizer injection. This result
coincides with the fact reported by Yuasa et al, that the fuel regression rate increased by 3 to 4 times in a swirling-
oxidizer-flow-type hybrid rocket as compared with the axial flow type hybrid rocket[1].

Kei Obata, Toru Shimada and Koki Kitagawa

From the result obtained in this analysis, the frequency of mode 2 coefficient is thought to have some relation with the oscillation frequency of the boundary layer. In particular, it will be a key to the frequency analysis of the boundary layer oscillation of hybrid rocket with swirling oxidizer flow. Further examination is needed in the analysis of the mode coefficient of the POD mode which captures periodic changes in luminous intensities of luminous flames.
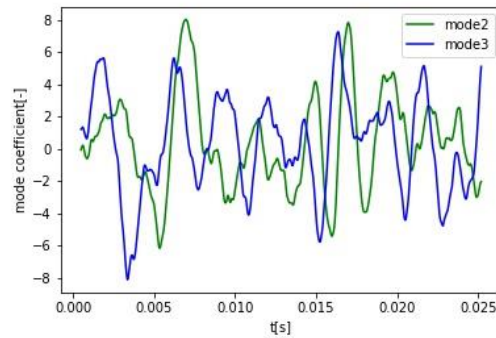
Figure 22: The trajectory of mode 2 and mode 3 coefficient, Se=30.0
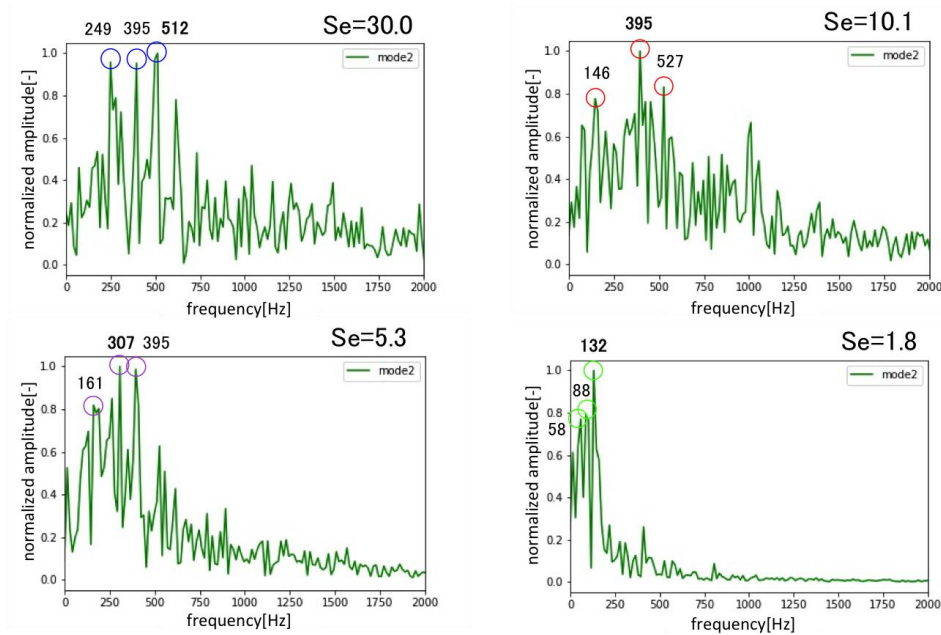
Figure 23: FFT results of the mode2 coefficient in different swirl intensities

Table 2: Analysis of 2nd POD mode coefficient frequency in different swirl intensities

Se (-)	30.0	10.1	5.3	1.8	0.0
2 mode (Hz)	512.7	395.5	307.6	131.8	102.5
Oscillation frequency of B.L (Hz)	129.7	118.6	112.7	107.2	110.4
Times (-)	3.95	3.33	2.73	1.23	0.93
τ_{bl2} **(ms)**	0.9	1.2	1.6	3.6	4.3

5. Conclusion

The elementary image analysis and proper orthogonal decomposition (POD) is applied to the images of luminosity taken from both the front and the side of combustion chamber of a new type of hybrid rocket, which has both tangential and radial oxidizer injection.

The swirling flame streaks made by dual injection are observed and axially distribution of their angles to horizontal is analysed. The intersection point of two decreasing curves moves to the injector side as the Se number increase. The flame zone thickness is also quantitatively estimated (7mm~10mm) and it is found to increase as the strength of swirl intensity increases.

The higher POD modes are found to capture the structures of luminous flame streaks. The peak frequency of mode 2 coefficient is found to have some relation with the oscillation frequency of the boundary layer. This is supported by two facts as follows: 1)The ratio of the peak frequency of the mode coefficient to the oscillation frequency of the boundary layer is close to 1.0 in the case of Se=1.8 and 0.0 and this ratio increases as the Se number increases. 2) In the case of only tangential oxidizer injection, the boundary layer delay time becomes four times at the maximum shorter than that of the case of only radial oxidizer injection.

Acknowledgments

References

[1] T. Tamura, S. Yuasa, K. Yamamoto. 1999. Effects of Swirling Oxidizer Flow on Fuel Regression Rate of Hybrid Rockets, *AIAA*, pp.1999-2323.

[2] K. Kitagawa, S. Yuasa. 2006. Combustion Characteristics of a Swirling LOX Type Hybrid Rocket Engine, *Journal of the Japan Society for Aeronautical and Space Science*, Volume 54, pp. 242-249.

[3] K. Ozawa, K. Kitagawa, T. Shimada. 2015. Performance Calculations and Burning Tests on Altering-intensity Swirling Oxidizer Flow Type Hybrid Rocket Engines, 66 th International Astronautical Congress.

[4] Elizabeth T. Jens, Victor A. Miller, Brian J. Cantwell. 2016. Schlieren and OH[*] chemiluminescence imaging of combustion in a turbulent boundary layer over a solid fuel, *Experiments in Fluids*, Volume 57, pp.16.

[5] M. Masugi, T. Ide, S. Yuasa, T. Sakurai, N. Shiraisi, T. Shimada. 2010. Visualization of Flames in Combustion Chamber of Swirling-Oxidizer-Flow-Type Hybrid Rocket Engines, *AIAA*, pp. 2010-6546.

[6] J.M. Beer, N.A. Chiger. 1972. Combustion Aerodynamics, *Applied Science*, pp. 106-107.

[7] P. Holmes, J.L. Lumley, G. Berkooz. 1998. Turbulence, Coherent Structures, Dynamical Systems and Symmetry, Cambridge University Press, Cambridge.

[8] M. Tanabe, M Saito, W.Z. Hallum.2016. Self-Excited Non-Linear Acoustic Wave in a Single-Element Model Rocket Combustor and Its Influence on Flame, JSASS, **14**, pp.1-6

[9] L. Sirovich. 1987. Turbulence and the dynamics of coherent structures part I: Coherent structures, Quarterly of applied mathematics, Vol.45, pp.561-571.

[10]   A. Mazzetti, P. Barbante. 2016. Numerical modeling of combustion processes in hybrid rocket engines, *International Journal of Energetic Materials and Chemical Propulsion*, Volume 15, pp.249-274.

[11]   K. Ozawa, T. Shimada. 2015. Flight Performance Simulations of Vertical Launched Sounding Rocket Using Altering-intensity Swirling Oxidizer Flow Type Hybrid Rocket Motors, *AIAA*, pp. 2015-3832.

[12]   K. Bizon, G. Continillo, E. Mancrauso. 2010. POD-based analysis of combustion images in optically accessible engines, *Combustion and Flame*, **157**, pp. 632-640.

[13]   K. Taira. 2011. Proper Orthogonal Decomposition in Fluid Flow Analysis: 1. Introduction, *Nagare*, **30**, 115-123

[14]   J.H. Tu, J. Griffin, A. Hart. 2013. Integration of non-time-resolved PIV and time-resolved velocity point sensors for dynamic estimation of velocity fields, Exp. Fluids, **54**, pp.1-20

[15]   G. Zillaic, M.A. Karabeyoglu.2006. Hybrid Rocket Fuel Regression Rate Data and Modeling, AIAA, pp. 2006-4504

[16]   A. Karabeyoglu. 2007. Combustion Instability and Transient Behavior in Hybrid Rocket Motors, Fundamentals of Hybrid Rocket Combustion and Propulsion, Progress in astronautics and aeronautics, Volume 218, pp.351-411